2018

Experimental test of decoherence theory using electron matter waves

Peter J. Beierle

Liyun Zhang

Herman Batelaan

PAPER • OPEN ACCESS

Experimental test of decoherence theory using electron matter waves

New Journal of Physics
The open access journal at the forefront of physics

Deutsche Physikalische Gesellschaft DPG
IOP Institute of Physics

Published in partnership with: Deutsche Physikalische Gesellschaft and the Institute of Physics

OPEN ACCESS

RECEIVED
26 August 2018

REVISED
24 October 2018

ACCEPTED FOR PUBLICATION
1 November 2018

PUBLISHED
21 November 2018

PAPER

Experimental test of decoherence theory using electron matter waves

Peter J Beierle[1], **Liyun Zhang**[2] **and Herman Batelaan**[1]

[1] Department of Physics and Astronomy, University of Nebraska-Lincoln, Lincoln, NE 68588, United States of America
[2] Key Laboratory of Quantum Information and Quantum Optoelectronic Devices, Xi'an Jiaotong University, Xi'an 710049, People's Republic of China

E-mail: hbatelaan2@unl.edu

Keywords: decoherence, quantum decoherence, electron diffraction, coherence length, surface decoherence, image charge, which-way information

Supplementary material for this article is available online

Abstract

A controlled decoherence environment is studied experimentally by free electron interaction with semiconducting and metallic plates. The results are compared with physical models based on decoherence theory to investigate the quantum-classical transition. The experiment is consistent with decoherence theory and rules out established Coulomb interaction models in favor of plasmonic excitation models. In contrast to previous decoherence experiments, the present experiment is sensitive to the onset of decoherence.

1. Introduction

The continuous divide between quantum and classical physics can be described by decoherence theory. Decoherence is an irreversible process in which a quantum state entangles with an environment in such a way that it loses its interference properties [1, 2]. For most experiments, maintaining a system's quantum coherence is desirable, and great efforts are made to isolate the system from its environment [3–6]. Additionally, it has been suggested that some sources of decoherence may be ubiquitous, such as those originating from vacuum field fluctuations or gravitation [7–12], and that decoherence, in general, is a critical element in resolving the quantum measurement problem [13]. Thus, experimentally sorting out various sources of decoherence and determining which dominate is desirable for both technical applications and fundamental studies, including the decoherence program [13].

There have been experiments in which the transition between the quantum and classical domain has been controlled through both the 'distance' between states [14–16] and the strength of the interaction with the environment [16–20]. Most of these experiments involve various matter-wave interferometric techniques.

In this work, we will describe a decoherence setup that is a realization of Zurek's original thought experiment of diffracting charges through a grating and controlling the spatial quantum coherence with a conducting surface [21]. We have measured the effect of a gold and silicon surface and found upper bounds on the loss of contrast due to decoherence. These results refute current decoherence models premised on image charge [22–24]. We also identify viable decoherence models based on dielectric excitation theory from effects including surface plasmons [25, 26].

In Sonnentag and Hasselbach's pioneering work, an electron biprism interferometer setup was used with separated arms passing over a semiconducting surface before recombination [16]. In contrast, we used electron diffraction from a nano-grating and measured the effect of a conducting surface. As we will show below, diffraction is well suited for measuring small losses in coherence, which is particularly useful to detect weak decoherence channels. Sonnentag's and Hasselbach's measurements on doped n-type silicon reveal a decoherence strength that is a factor of $\approx 10^2$ too weak as compared to Zurek's image charge model. This is confirmed by our findings.

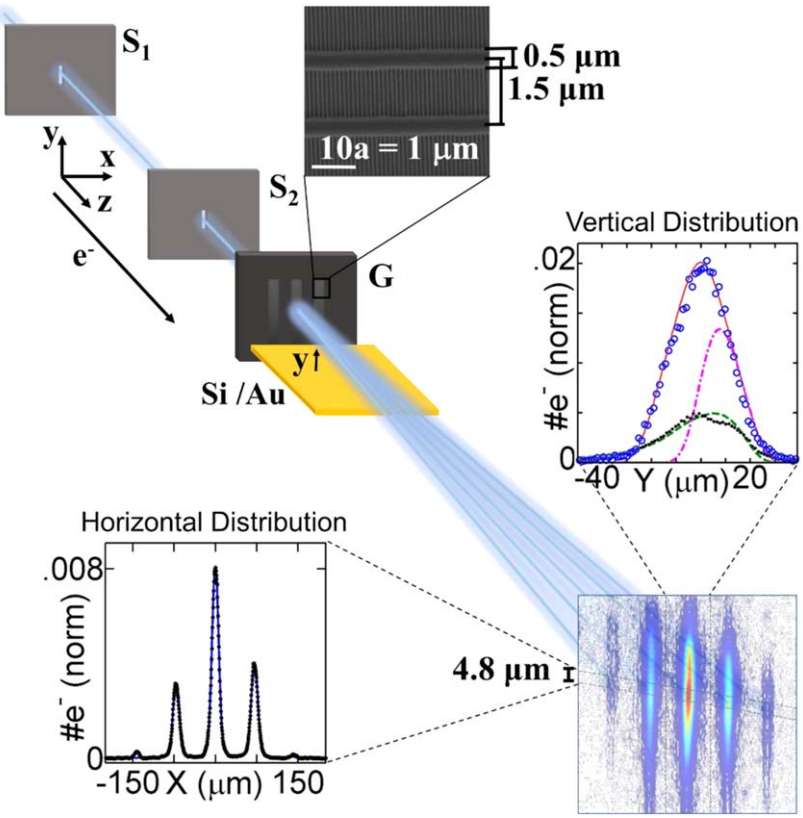

Figure 1. Experimental setup. Electrons are prepared in a spatially coherent state by collimation with two slits (S_1 and S_2), then diffracted through a nanofabricated diffraction grating (G) before passing over either a doped Silicon (Si) or Gold (Au) surface, which acts as the 'environment'. Inset-top: an electron microscope image of the diffraction grating shows the 100 nm periodicity and the 0.5 μm support structure of the grating bars. Middle-right: electron distribution in the y-direction taken when there is no surface (solid red line) compared to when the surface is raised to cut 2/3 of the beam (dashed and dotted–dashed lines). The distribution in the y-direction (black solid data points as in the case of gold) closely fits the simulation when image charge is present (dashed green line) as opposed to no image charge (dashed–dotted magenta line). See appendix A and figure A2 for information on the relationship between Y and the height of the beam over the surface. Bottom left: an electron diffraction pattern and a fit are shown.

The determination of the physical mechanism nevertheless supported image charge models [16, 23] as the analysis ignored the strength of decoherence and was limited to a best fit of the functional form, as was done in a similar experiment by Röder and Lubk [27]. The implicit assumption is that a metallic surface (as used in the theory) behaves similarly as a silicon surface. The image charge models were thus considered valid. Our measurements, which now also includes the conductor gold as well as silicon, refutes this conclusion and identifies Howie's model [25, 26] as viable.

2. Experimental setup

A 1.67 keV electron beam (Kimball EGG-3101 electron gun) is sent through two collimation slits separated by 25 cm with a geometrical beam divergence of 61 μrad in the x-direction and 120 μrad in the y-direction (see figure 1). This collimation gives a transverse coherence length of the electron beam of approximately 600 nm as determined by diffraction images. This makes it possible to diffract the electrons from a 100 nm periodic nanofabricated grating [28, 29]. The transverse coherence length of the electron beam in the vertical direction (~300 nm) is smaller than to the periodicity of the support structure (~1 μm, equation (1)). The diffraction order separation in the y-direction (~5 μm) at the detector is much less than the 1 beam height (~30 μm). The diffraction broadening in the vertical direction is thus negligible. The vertical height of the gratings (>1 mm) is much larger than the electron beam height and poses no further constraints. The diffracted electron distribution is magnified 24 cm downstream by an electrostatic quadrupole lens, detected by a multichannel plate detector, backed by a phosphorous screen (Beam Imaging Solutions BOS-18), and imaged by a CCD camera. A LabVIEW image acquisition program [30] accumulates a two-dimensional streaming image from the camera. The vacuum chamber in which this experiment takes place is held at a pressure of $\approx 4 \times 10^{-5}$ Pa and is protected from external magnetic fields by two layers of mu-metal magnetic shielding.

A 1 cm^2 silicon or gold (Si/Au) surface is then brought in from below the diffracted beam 3 mm after the grating such that the surface in the x–z plane is perpendicular to the diffraction grating bars. The surface height is adjusted to cut into the beam so that 1/3 of the intensity of the original beam reaches the detector. The surface is supported by a mechanical feedthrough whose angular pitch with respect to the beamline can be adjusted with a precision of approx. 0.2 mrad. This pitch of the surface is adjusted to maximize the electron beam's deflection due to image charge attraction. This gives rise to a tail in the diffraction image that extends to below the plane of the surface ($y < 0$). No electrons were observed that moved with the surface angle, which rules out significant contribution of elastically reflected electrons. The Si surface was cleaned using a version of the industry-standard RCA cleaning method (without the oxide strip) [31], to remove dust or other contaminants.

Two-dimensional images of the electron diffraction pattern are recorded (figure 1, bottom right). The diffraction pattern that is roughly aligned with the horizontal x-direction was analyzed by taking cross-sections of the image along a slanted horizontal line that matches the slant of the diffraction pattern and averaging vertically 5 pixels (an example labeled with 4.8 μm in the Y-direction on the detection screen). This we call a 'line-out'.

3. Measuring effects of decoherence in terms of transverse coherence length

When an electron passes over a decohering surface, it interacts with the surface so that the interference pattern in the far field has lower visibility, and further decreases the closer the electron passes over the surface. Previously, the decoherence was measured in terms of the visibility of the interference pattern [14, 16, 18, 27], i.e. $V_{is} = (I_{max} - I_{min})/(I_{max} + I_{min})$.

However, in order to be sensitive to small changes in contrast and reduce the uncertainty in measurement due to background counts, we use a measure of the transverse coherence length of the diffracted beam in terms of the observed width of the diffraction peaks w_{FWHM} at the detector [32]:

$$L_{coh} \approx \frac{\lambda_{dB}}{\theta_{coll}} \approx \frac{ad}{w_{FWHM}}. \tag{1}$$

Here a is the periodicity of the grating, d is the distance between neighboring diffraction peaks at the detection screen, θ_{coll} is collimation angle of the electron beam, and w_{FWHM} is the FWHM of a diffraction peak.

Thus, here we associate a loss of coherence with an increase of the width of the diffraction peaks w_{FWHM} rather than a loss of visibility. For the theoretical models, the predicted width w_{FWHM} increase will be due solely to decoherence; while for the experiments the observed increase of width leads to an upper limit on decoherence, as other process may also increase w_{FWHM}, such as dephasing [33]. Dephasing is caused by time-reversible processes, while decoherence is caused by time-irreversible processes ([33] and references therein).

The advantage of using diffractometry over interferometry lies in their respective decoherence measures, L_{coh} and V_{is}. The background signal can be subtracted for diffraction without distorting the measured value of L_{coh}. This is not the case when measuring visibility in an interferometer. The interference pattern's visibility V_{is} drops off linearly due to a weak background signal, which can mask decoherence (see figure 2). For a weak decohering environment that scatters the incident beam and introduces background, diffractometry is thus well suited.

In our experiment, the electron diffraction pattern are recorded (figure 1, bottom right). The diffraction line-outs are modeled by,

$$I(x) = \left\{\frac{\sin[\alpha(x - x_0)]}{\alpha(x - x_0)}\right\}^2 \left[\sum_{n=0} G(x - x_1 \pm nd)\right] + A_{bckd} \exp[-(x - x_2)^2/2c_3^2], \tag{2}$$

where the first term corresponds to the diffraction peaks weighted by the single slit envelope. The single slit envelope is centered at x_0 with a width controlled by the parameter α, x_1 is the center position of the 0th order diffraction peak and$d$ d is the peak periodicity. The diffraction peaks,

$$G(x) = a_1 e^{-x^2/2c_1^2} + (1 - a_1) e^{-x^2/2c_2^2}, \tag{3}$$

are all approximated by two Gaussians with overlapping means, with relative intensities a_1 and $1 - a_1$, and standard deviations c_1 and c_2. This function fits the shape of the beam well. The peak to peak distance is d. The zeroth order diffraction peak is centered at x_1. The second term in equation (2) corresponds to a background with an amplitude of A_{bckd}, centered at x_2, and has a standard deviation of c_3. From this fit the w_{FWHM} and d are extracted to compute the coherence length L_{coh} for a given distribution according to equation (1).

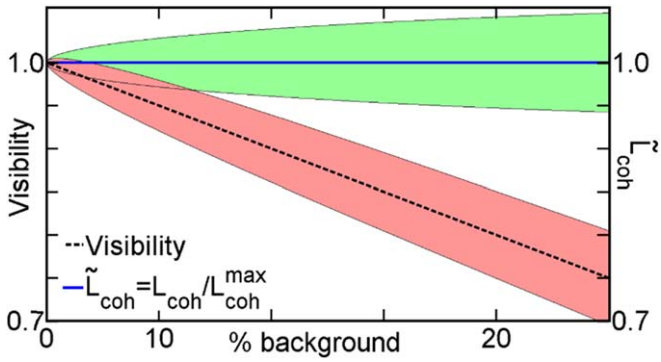

Figure 2. Comparison between visibility (V) and normalized transverse coherence length ($\tilde{L}_{\rm coh} = L_{\rm coh}/L_{\rm coh}^{\rm max}$). For interferometry, the visibility is used to place a bound on decoherence. For diffraction, the decoherence measure is coherence length. The advantage of using diffraction rather than interferometry is that the decoherence measure is not background dependent. In other words, the linear drop of visibility in an interferometer (dashed line) due to a weak background signal masks the decoherence. This makes diffraction well suited to search for weak decoherence. The shaded areas correspond to uncertainty due to the statistical error introduced by the background.

4. Surface-induced decoherence models

There are various models that predict different coherence lengths as a function of height above the surface, and material properties of the surface. The original model that focused on electron-surface decoherence was conceived of by Anglin and Zurek [21, 22]. The physical system is a classical image charge on the surface of the conductor that follows the free electron as it travels parallel to the surface. Joule heating, experienced by the image charge while traversing the surface, causes dissipation with a relaxation time $\tau_{\rm relax}$. Back-action on the free electron leads to decoherence with a corresponding time $\tau_{\rm dec}$ (called decorrelation time in [34]). The decoherence time is taken to be proportional to the relaxation time according to [34],

$$\tau_{\rm dec} = \left(\frac{\lambda_{\rm th}}{\Delta x}\right)^2 \tau_{\rm relax}, \tag{4}$$

where $\lambda_{\rm th}$ is the thermal de Broglie wavelength of the image charge, and Δx is the distance between decohering paths associated with the electron moving over the surface. the relaxation time due to Ohmic dissipation is $\tau_{\rm relax} = 16\pi m y^3/e^2\pi\rho$. Thus, according to this model, the resulting decoherence timescale is [35],

$$\tau_{\rm dec}^{\rm Zurek} = \frac{4h^2}{\pi e^2 k_{\rm B} T\rho}\frac{y^3}{(\Delta x)^2}, \tag{5}$$

where ρ corresponds to the resistivity of the surface material and e is the electron's charge, y is the height of the electron over the surface, m is the mass of the electron, $k_{\rm b}$ is Boltzmann's constant, and T is the temperature of the surface (room temperature).

The decoherence model by Scheel and Buhmann [24] is also based on the electron's interaction with its image charge, but it considers a full 'macroscopic quantum electrodynamics' treatment. This takes into consideration the surface's linear dielectric response. Taking the low-frequency limit where the Drude approximation $\varepsilon(\omega) \approx 1 + i/(\varepsilon_0\rho\omega)$ holds for both gold [24] and doped silicon [25, 36], the decoherence timescale is,

$$\tau_{\rm dec}^{\rm Buhmann} = \frac{\pi\varepsilon_0\hbar^2}{e^2 k_{\rm B} T\rho}\left[\frac{1}{2y} - \frac{1}{\sqrt{(2y)^2 + (\Delta x)^2}}\right]^{-1}. \tag{6}$$

In the limit $\Delta x \ll y$, this is equivalent to equation (5), which underlines the similarity of the physical mechanisms of the above two models.

While these models posit to hold for a wide range of materials (including semiconductors and metals) Howie's model [25] is worked out only for semiconductors and Machnikowski's model [23] is only worked out for metals. Howie's model is based on event probability e^{-P} rather than energy dissipation, where such events correspond to 'aloof scattering' with long wavelength plasmons and 'similar excitations' up to a cutoff frequency $\omega_m = 0.6 \times 10^{12}$ Hz [25]. The expression for this probability for a path length L is,

$$P^{\rm Howie} = \left(\frac{e^2 L\omega_m^2}{4\pi^2\hbar\sigma v^2}\right)\int_{y/4\Delta x}^{\infty}\frac{\exp(-s)}{s}{\rm d}s, \tag{7}$$

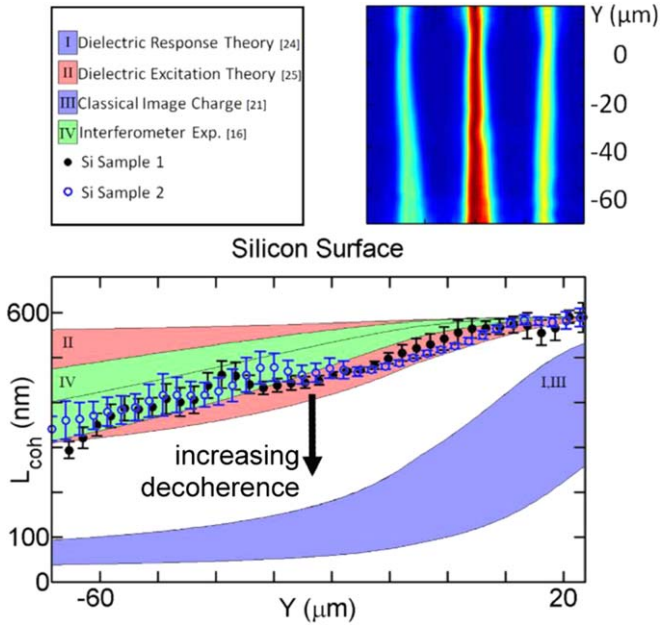

Figure 3. Theoretical transverse coherence length and experimental limits for a silicon surface. The diffraction pattern (top right) shows a loss of contrast as the diffraction peaks broaden for electrons that passed close to the surface, as observed in the broadening of the diffraction peaks as a function of vertical position on the detector. Our experimental findings (dotted) show agreement with Hasselbach's experimental fit (IV, green), and might be consistent with modeling based on dielectric excitation theory (II, red). The experimental increase in observed width (related to coherence length by equation (1)) can be due to decoherence or dephasing and is an upper limit on the amount of decoherence. Theoretical models that predict more decoherence (with a predicted coherence length smaller than the experimental data) are in disagreement with the experiment. The data does not agree with models based on Ohmic dissipation due to classical image charge and macroscopic quantum electrodynamic theory using dielectric response (I and III, blue).

where L is the length of the surface, σ is the conductivity of the surface v and is the velocity of the electron in the z-direction [25]. We approximate the exponential integral by [37],

$$-Ei(-\eta) = \int_{\eta}^{\infty} \frac{\exp(-s)}{s} \mathrm{d}s \cong (A^{-7.7} + B)^{-0.13}, \tag{8}$$

where $\eta = y/4\Delta x$ [38][3], $A = \log[(0.56146/\eta + 0.65)(1 + \eta)]$ and $B = \eta^4 e^{7.7\eta}(2 + \eta)^{3.7}$. Note that we did not include any Boltzmann correction factor [38] (see footnote 3), nor did we analyze the relative strength of relativistic and non-relativistic terms in the aloof beam interaction [25, 26].

Machnikowski's fully quantum many-body electron gas model infers that the primary decoherence mechanism is due to the dissipative effects of image charge formation rather than Ohmic resistivity effects [23]. It is dependent on the Fermi wave-vector for metals (k_{Fermi}). The decoherence timescale is,

$$\tau_{\mathrm{dec}}^{\mathrm{Machnikowski}} = \frac{32\varepsilon_0 h^2 k_{\mathrm{Fermi}}}{\pi e^2 m k_{\mathrm{B}} T}\left(\frac{y}{\Delta x}\right)^2. \tag{9}$$

For all of the above models, decoherence over the surface modifies the density matrix of the electron according to [1, 39]:

$$\rho_{\mathrm{final}} = \rho_{\mathrm{initial}} e^{-\int_{t_i}^{t_f} \mathrm{d}t/\tau_{\mathrm{dec}}} = \rho_{\mathrm{initial}} e^{-\Gamma}, \tag{10}$$

where Γ is the decoherence factor and the decoherence timescale τ_{dec} is not only model-dependent but also depends on Δx and y. For all of the models, the diffraction pattern is obtained by propagating the final density matrix to the detection screen (see appendix A3 for details). The change in transverse coherence length is then obtained from the calculated far-field diffraction pattern using equation (1).

5. Results

Plotted in figure 3 is a comparison of the coherence length as a function of height for the case of two different n-type phosphorous doped silicon samples of resistivities 1–20 Ω cm and 1–10 Ω cm (solid black data points and hollow blue data points respectively). The experimental reduction in coherence length can be due to

[3] Note that the original publication has a typo in placing the factor of 4 in the numerator.

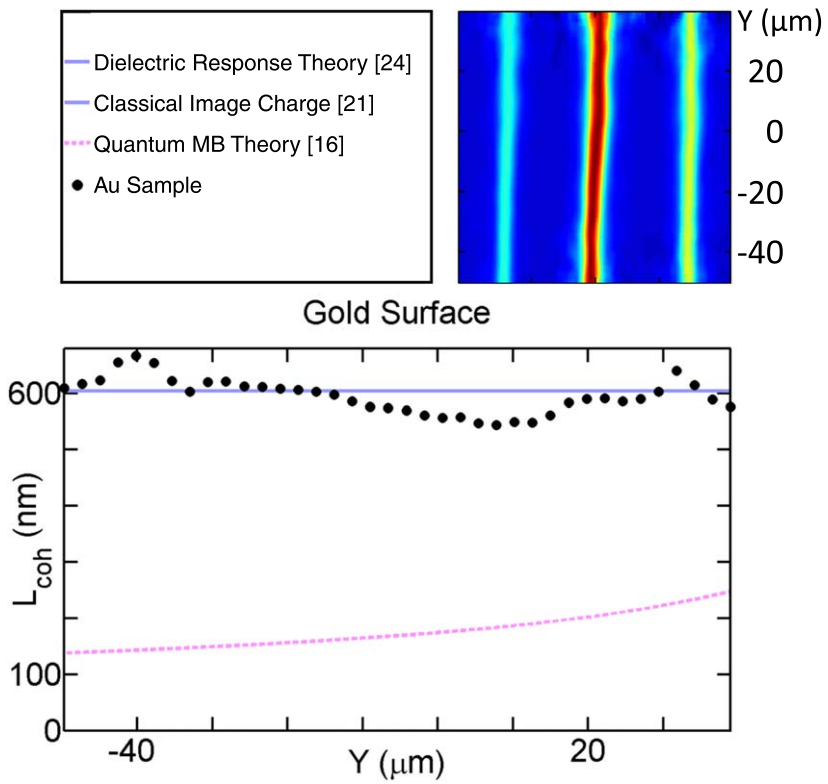

Figure 4. Transverse coherence length for a gold surface. The diffraction pattern shows no loss of contrast for electrons that passed close to the surface, as observed in the broadening of the diffraction peaks as a function of vertical position on the detector (top right). The data does not agree with the image charge formation model in a quantum many-body electron gas model (dashed line, pink). The predicted decoherence is too strong and can be ruled out.

decoherence and/or dephasing [33] and is an upper limit on the amount of decoherence. Our results agree with Hasselbach's experimental findings, who used a 1.5 Ω cm n-type doped silicon sample of 1 cm length using the same beam energy of 1.67 keV. To compare our data with these findings, we substituted Sonnentag fitted function $\{\exp[-a(\Delta x/\mu m)^2/(z/\mu m)^3]\}$ into equation (10), where $a = 10.9$ and the upper and lower bounds of the green region of figure 3 correspond to the reported +13.6 and −5.8 uncertainties [16]. The observed loss of contrast can be visualized in the diffractogram's diffraction peak broadening (figure 3 top right), based on the histogram data collected from the CCD camera (see appendix B for more details).

The experimental data is also compared to Zurek's model of classical image charge/Ohmic dissipation, Scheel and Buhmann's macroscopic quantum electrodynamic model and Howie's dielectric excitation theory model. The uncertainty associated with the theoretical curves (shaded regions I, II and III) in figure 3 corresponds to the range of Si resistivity 1–20 Ω cm. The shaded region for Hasselbach's experimental fit (IV) corresponds to the published experimental uncertainty [16]. The observed loss of contrast in doped silicon rules out Zurek's and Scheel's decoherence models. This is in contrast to the claim made earlier that Zurek's model is in adequate agreement with experiment [16]. Even if dephasing is present in our experiment, the observed loss of contrast is much smaller than predicted by the models and therefore the conclusion remains valid. Howie's dielectric excitation model is in agreement with our findings.

This experiment was also carried out for the case of a gold surface and plotted in figure 4 is the transverse coherence length as a function of height. For a metal with a resistivity of 2.2×10^{-6} Ω cm [40], no reduction, in contrast, is measured for an electron passing close to the gold surface. This is consistent with Zurek's and Scheel & Buhman's models. Machnikowski's image charge formation model significantly overestimates the loss of coherence, despite being developed for high conductivity metals such as gold. Hence, Machnikowski's model can also be ruled out as a viable decoherence mechanism.

The general lack of height-dependence of the loss of contrast can be visualized in the diffraction peak's width of the diffraction pattern remaining approximately constant (figure 4 top right). This height independence of the coherence length for the case of the gold surface contrasts that of doped silicon. This may be connected to the much smaller resistivity of gold than doped silicon. No theoretical model is currently able to explain both results.

6. Outlook and conclusion

This nano-grating diffraction setup opens the door to more sensitive measurements of weak decoherence results. Consider that our modest experimental setup is limited by an initial coherence width (≈600 nm) and that the decoherence factor in many cases scales as $(\Delta x)^2$. Given that it is now possible for transmission electron microscopes to reach coherence lengths as large as 100 μm [41], the sensitivity can thus be improved by $\approx 10^4$. The general method of detection present here opens the pathway to study spatially dependent decoherence surface effects due to plasmon excitation [25, 26, 42], optical bandgap excitation, superconductive transitions, spin-dependent transport effects [43–45], coherent thermal near-fields [46–48], blackbody-like near-fields [49, 50], etc.

There has been much interest in the potential to measure the effects of decoherence due to vacuum field fluctuations in electron interference [7–10, 51–53]. It has been shown that, absent of the surface, the decoherence factor scales with $\Gamma \sim (\Delta x)^2/(c^2 T_{\rm flight}^2)$ where $T_{\rm flight}$ is the total time of flight of the electron [8, 53]. Given that Δx is generally between 100 nm and 100 μm and $T_{\rm flight}$ is roughly between 1 and 100 ns, this corresponds to a transverse velocity of $v_T \equiv \Delta x/T_{\rm flight} \sim 10^5$ m s^{-1} and a decoherence factor of $\sim 10^7$, which is not currently feasible to observe. To observe such decoherence, the transverse velocity has to be increased by changing the experimental configuration (for example as in a quantum electron microscope [54, 55]).

In conclusion, we have confirmed the loss of contrast in an electron diffraction pattern due to the introduction of a doped silicon surface with a strength consistent with Sonnentag and Hasselbach's biprism interferometer experiment. Our diffractometer setup is simpler in terms of its components and is particularly advantageous in observing weak decoherence effects. Thus, we have shown a new pathway to observe weak decoherence channels. Additionally, for the case of a gold surface, we have placed an upper bound on the loss of contrast that can be attributed to decoherence. The silicon and gold decoherence results together confirm that the observed effect is strongly material dependent. We have ruled out a range of decoherence models due to image charge based on classical theory [22], quantum many-body theory [23], and dielectric theory [24]. For the materials and electron beam parameter range studied, our work might be consistent with decoherence effects due to dielectric excitation theory from effects including surface plasmons [25, 26]. These findings are consistent with the general decoherence program [1, 2, 13].

We thank Vijay Singh, Keith Foreman and Stephen Ducharme for their help in surface preparation. Characterization analysis was performed at the NanoEngineering Research Core Facility (NERCF), University of Nebraska-Lincoln. This work was completed utilizing the Holland Computing Center of the University of Nebraska, which receives support from the Nebraska Research Initiative. We gratefully acknowledge support by the US National Science Foundation under Grant No. 1602755.

Appendix A. Theoretical method

A1. Introduction

In order to compute the final coherence length as a function of height Y on the far field detector as predicted by the various physical models, we used a combination of simulating classical trajectories in the y-direction and evolution of the electron's density matrix in the x-direction as it passes over the surface. The z-direction propagation is given by $z = vt$ (see figure 1 in the main paper). The motivation for separating the motion in a classical and quantum part is that the electron beam collimation slits are tall in the y-direction and yield a very small transverse coherence length, justifying a classical approach for motion in the y-direction. In the x-direction, the slits are narrow and yield a coherence length wider than the grating periodicity, necessitating a quantum approach as intended by the design of the experiment.

A2. Comparison between the measured vertical electron distribution and classical image charge force simulation

By simulating classical trajectories in the y–z plane, we can match the distribution of trajectories to the experimentally measured intensity distribution at the detector (figure A1). Starting with a distribution of initial positions and momentum defined by the 1st and 2nd slits, the trajectories over the surface are computed in time-steps including an image charge force on the electrons in the y-direction. The surface cuts into the electron beam so that only 1/3 of the original electron beam flux makes it to the detector. The electron's free propagation between the surface and the detector is computed and the position on the detector is binned and recorded. This classical simulation well approximates what is observed experimentally at the detector (figure A1). For reference, based on the simulated trajectories, the vertical position of the electron as it lands on the detector between $-70\ \mu\text{m} < Y < 20\ \mu\text{m}$ corresponds to an average height of the electron traversing over the surface between $1.75\ \mu\text{m} < y < 9.5\ \mu\text{m}$.

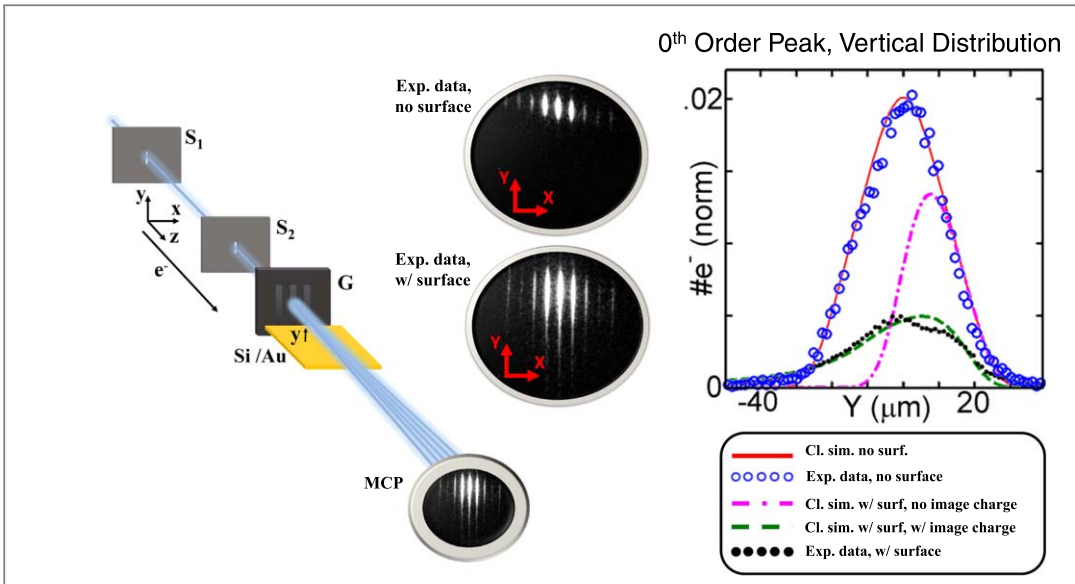

Figure A1. Electron distribution in the *y*-direction on the detector. Left: experimental setup. Middle: images of the accumulated diffraction patterns. The case without a surface (top) is compared to when the surface is raised to cut 1/3 of the beam (bottom). Right: electron distribution of the 0th order diffraction peak at the detection screen in the *Y*-direction. The case without the surface (plotted with blue rings) compared to with the surface (plotted with black dots). The distribution in the *y*-direction closely fits the classical simulation when image charge is present (dashed green line) as opposed to when no image charge is present (dashed–dotted magenta line).

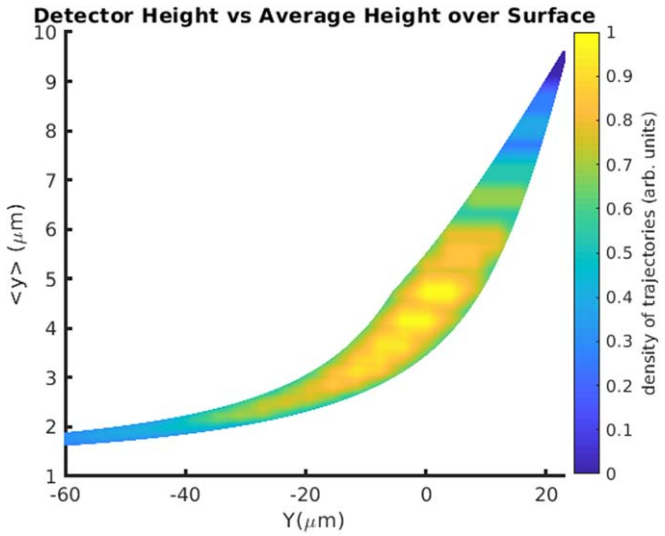

Figure A2. Height relation. The vertical height of the electrons on the detection screen (*Y*) is given as a function of the average height (*y*-value) of trajectories above the surface. The trajectory heights are obtained from a classical simulation. Bright yellow (dark blue) corresponds to a high (low) electron trajectory density.

A3. Calculating the theory-predicted change in transverse quantum coherence length using the density matrix formalism and fourier transformations

To calculate the change in transverse coherence length predicted by the theories in the literature, we first prepare the initial density matrix of the free electron by considering a partially coherent Gaussian beam,

$$\rho(x, x') = \frac{1}{\sigma_0^{\mathrm{coh}}\sqrt{2\pi}} \exp\left[-(x - x_0)^2/2(\sigma_0^{\mathrm{coh}})^2\right] \times \exp\left[-(x')^2/2(\sigma'_{\mathrm{initial}})^2\right]. \tag{A.1}$$

Here x and x' describe the coordinates of the matrix element in the direction of the diagonal and in the direction orthogonal to the diagonal respectively (figure A3). The position x_0 indicates the center of the Gaussian. The width of the Gaussian in the x'-direction, $w'_{\mathrm{initial}} \equiv 2\sqrt{2\ln(2)}\,\sigma'_{\mathrm{initial}}$, is proportional to the transverse coherence length. The spatial width along x, $w \equiv 2\sqrt{2\ln(2)}\,\sigma_0^{\mathrm{coh}}$ is determined by a path integral simulation taking into consideration propagation through the first two collimation slits and reaching the beginning of the surface [28].

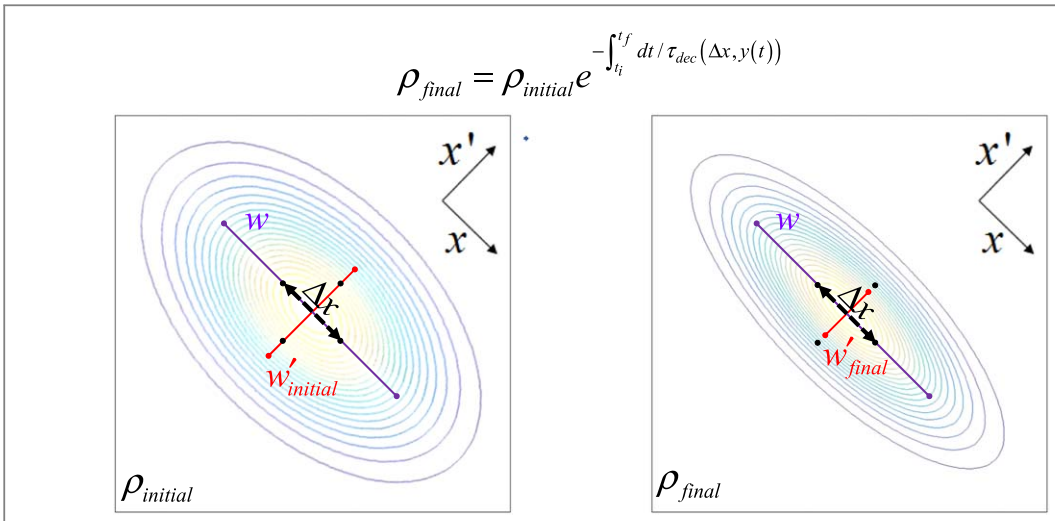

Figure A3. Evolution of density matrix. As a result of decoherence, the initial state (left) evolves such that the off-diagonal elements reduce in amplitude. Hence the state's width w' decreases (right).

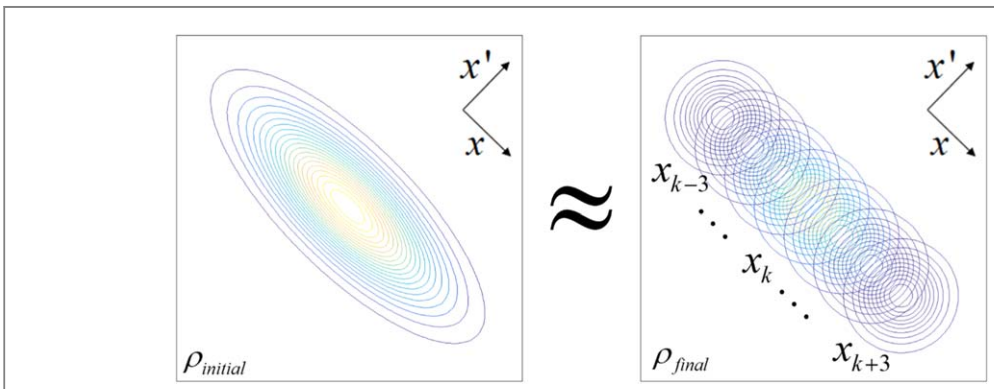

Figure A4. Deconvolution of a partial coherent (mixed) state by a series of coherent (pure) states.

Note that if w'_{initial} equals w, then the initial beam is fully coherent. If w'_{initial} is smaller than w, then the initial beam is partially coherent as in figure A3 (left). The initial state of the electron ρ_{initial} describes the electron before interacting with the surface at time t_i.

Now we consider the electron interaction with the surface. We model the change in transverse coherence length due to the interaction from a given decoherence process by considering the evolution of the density matrix of the electron. It changes according to [39]:

$$\rho_{\text{final}} = \rho_{\text{initial}} e^{-\int_{t_i}^{t_f} \text{dt}/\tau_{\text{dec}}}, \tag{A.2}$$

where the decoherence timescale τ_{dec} is model-dependent, and depends on Δx and $y(t)$. When computing the integral in equation (A.2), the simulated trajectories $y(t)$ are inserted.

Each element in the density matrix is computed according to equation (A.2). The distance between paths Δx used in the models equals the distance between the corresponding off-diagonal terms in the density matrix (figure A3). The final state of the electron ρ_{final} is now found right after the interaction with the surface at time t_f. The density matrix of the electron has the form,

$$\rho_{\text{final}}(x, x') = \frac{1}{\sigma_0^{\text{coh}}\sqrt{2\pi}} \exp\left[-(x - x_0)^2/2(\sigma_0^{\text{coh}})^2\right] \times \exp\left[-(x')^2/2(\sigma'_{\text{final}})^2\right], \tag{A.3}$$

where the width of the final state orthogonal to the diagonal is smaller than the width of the initial state ($w'_{\text{final}} < w'_{\text{initial}}$). This step describes decoherence.

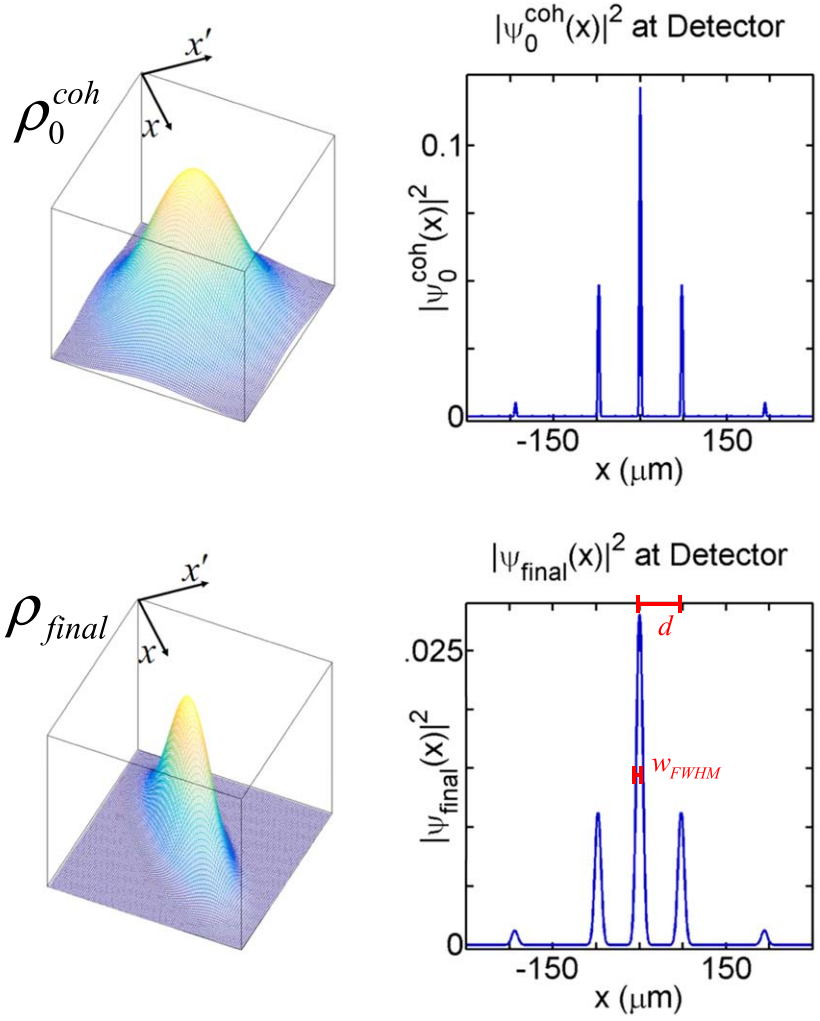

Figure A5. Coherence reduction. Top left: density matrix of a coherent Gaussian electron beam. Top right: grating diffraction pattern in the far field after Fourier transformation of the coherent state. Bottom left: final density matrix after decoherence evolution according to equation (A.2). Bottom right: grating diffraction pattern in the far field after Fourier transformation of the deconvoluted partial coherent state.

Making use of the ability to write a partial coherent state as a sum of coherent (i.e. pure) states (see figure A4),

$$\rho_{\text{final}} = \sum_{n=1}^{\infty} c_n \rho_n^{\text{coh}}, \tag{A.4}$$

then we can write ρ_{final} as a sum of Gaussian coherent states,

$$\rho_{\text{final}} \approx \sum_{n=1}^{N} \exp[-(x - x_n)^2/2(\sigma_{\text{env}})^2] \times \exp\{-[(x - x_0 - x_n)^2 + (x')^2]/2(\sigma_2^{\text{coh}})^2\}, \tag{A.5}$$

where $\sigma_2^{\text{coh}} = \sigma'_{\text{final}}$ describes the width of the reduced pure states after decoherence and

$$\sigma_{\text{env}} = \sqrt{(\sigma_0^{\text{coh}})^2 - (\sigma_2^{\text{coh}})^2}, \tag{A.6}$$

is the width of the envelope of the convolution. The infinite sum in equation (A.4) is approximated numerically with a finite sum in equation (A.5).

Next, each wave function corresponding to one of the reduced pure states is acted upon by a grating function. A Fourier transform is used to determine the far field pattern. This is repeated for each of the reduced pure states and the resulting probability distribution patterns are summed to give the final far field diffraction pattern (figure A5 bottom right). It is from this final pattern that a transverse coherence width $L_{\text{coh}}(\text{Y})$ is computed using

$L_{\text{coh}} \approx \lambda_{dB}/\theta_{\text{coll}} \approx ad/w_{\text{FWHM}}$, where a is the periodicity of the grating, w_{FWHM} is the width of the computed diffraction peaks in the far field, and d is the distance between diffraction peaks . It is these values $L_{\text{coh}}(\text{Y})$ which produce the theoretical curves in the figures 3 and 4 in the main paper.

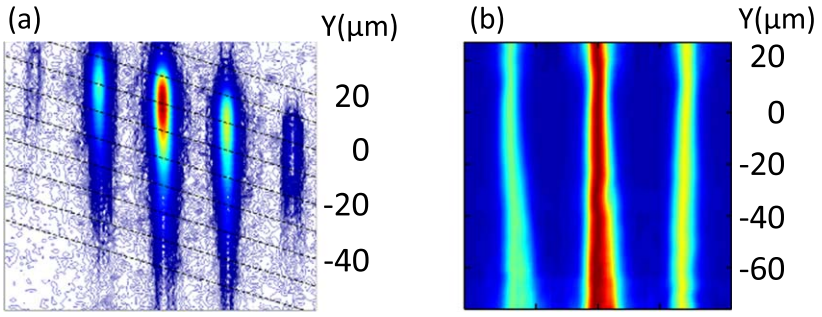

Figure B1. Visualization of the loss of contrast. (a) Contour of data accumulated by CCD camera. (b) Resulting diffractogram based on data.

Appendix B. Visualization of Loss of Coherence

In order to highlight the loss of contrast in the diffraction pattern, the accumulated image of the MCP detector that was taken by the CCD camera was transformed into the revised images shown in figures 2 and 3 in the main paper. Figure B1 shows the images before and after this process. Line-outs of the image are extracted to obtain diffraction patterns. The line-outs are taken at a slant with the x-direction to compensate for image skew. This skew can be explained by small rotational misalignments between the optical elements in the system, however this does not affect the measured coherence length. In the y-direction a 4.8 μm range on the detector is integrated for each line-out. Each of these line-outs then correspond to an individual horizontal line on the diffractogram.

After the individual line-outs are fitted according to equation (2) in the main paper, the background term is subtracted from the line-out to show only the relative broadening. Each diffraction peak is normalized by its maximum intensity value for that order.

ORCID iDs

Peter J Beierle https://orcid.org/0000-0001-5547-9897
Herman Batelaan https://orcid.org/0000-0003-3175-8095

References

[1] Zurek W H 2003 *Rev. Mod. Phys.* **75** 715
[2] Giulini D, Joos E, Kiefer C, Kupsch J, Stamatescu I-O and Zeh H D 1996 *Decoherence and the Appearance of a Classical World in Quantum Theory* (Berlin: Springer)
[3] Kuhr S *et al* 2007 *Appl. Phys. Lett.* **90** 164101
[4] Lewandowski H J, McGuirk J M, Harber D M and Cornell E A 2003 *Phys. Rev. Lett.* **91** 240404
[5] Pellizzari T, Gardiner S A, Cirac J I and Zoller P 1995 *Phys. Rev. Lett.* **75** 3788
[6] Unruh W G 1995 *Phys. Rev.* A **51** 992
[7] Ford L H 1993 *Phys. Rev.* D **47** 5571
[8] Breuer H-P and Petruccione F 2001 *Phys. Rev.* A **63** 032102
[9] Levinson Y 2004 *J. Phys. A: Math. Gen.* **37** 3003
[10] Hsiang J-T and Ford L H 2009 *Int. J. Mod. Phys.* A **24** 1705
[11] Penrose R 1996 *Gen. Relativ. Gravit.* **28** 581
[12] Pikovski I, Zych M, Costa F and Brukner Č 2015 *Nat. Phys.* **11** 668
[13] Schlosshauer M 2005 *Rev. Mod. Phys.* **76** 1267
[14] Brune M, Hagley E, Dreyer J, Maître X, Maali A, Wunderlich C, Raimond J M and Haroche S 1996 *Phys. Rev. Lett.* **77** 4887
[15] Myatt C J *et al* 2000 *Nature* **403** 269
[16] Sonnentag P and Hasselbach F 2007 *Phys. Rev. Lett.* **98** 200402
[17] Friedman J R, Patel V, Chen W, Tolpygo S K and Lukens J E 2000 *Nature* **406** 43
[18] Hornberger K, Uttenthaler S, Brezger B, Hackermüller L, Arndt M and Zeilinger A 2003 *Phys. Rev. Lett.* **90** 160401
[19] Hackermüller L, Hornberger K, Brezger B, Zeilinger A and Arndt M 2004 *Nature* **427** 711
[20] Akoury D *et al* 2007 *Science* **318** 949
[21] Anglin J R, Paz J P and Zurek W H 1997 *Phys. Rev.* A **55** 4041
[22] Anglin J R and Zurek W H 1996 *Dark Matter in Cosmology—Quantum Measurements Experimental Gravitation* (Savoie: Editions Frontieres) pp 263–70
[23] Machnikowski P 2006 *Phys. Rev.* B **73** 155109
[24] Scheel S and Buhmann S Y 2012 *Phys. Rev.* A **85** 030101
[25] Howie A 2011 *Ultramicroscopy* **111** 761
[26] Howie A 2014 *J. Phys.: Conf. Ser.* **522** 012001

[27] Röder F and Lubk A 2014 *Ultramicroscopy* **146** 103
[28] Gronniger G, Barwick B, Batelaan H, Savas T, Pritchard D and Cronin A 2005 *Appl. Phys. Lett.* **87** 124104
[29] Barwick B, Gronniger G, Yuan L, Liou S-H and Batelaan H 2006 *J. Appl. Phys.* **100** 074322
[30] Bach R, Pope D, Liou S-H and Batelaan H 2013 *New J. Phys.* **15** 033018
[31] Itano M, Kern F W, Miyashita M and Ohmi T 1993 *IEEE Trans. Semicond. Manuf.* **6** 258
[32] Cronin A D, Schmiedmayer J and Pritchard D E 2009 *Rev. Mod. Phys.* **81** 1051
[33] Chen Z, Beierle P and Batelaan H 2018 *Phys. Rev.* A **97** 043608
[34] Zurek W H 1986 *Front. Nonequilibrium Stat. Phys.* ed G T Moore and M O Scully (New York: Springer US) pp 145–9
[35] Sonnentag P 2006 Ein experiment zur kontrollierten Dekohärenz in einem Elektronen-Biprisma-Interferometer *PhD Thesis* University of Tübingen
[36] van Exter M and Grischkowsky D 1990 *Appl. Phys. Lett.* **56** 1694
[37] Giao P H 2003 *Groundwater* **41** 387
[38] Howie A and Beierle P 2017 private communication
[39] Breuer H-P and Petruccione F 2002 *Theory Open Quantum Syst.* (Oxford: Oxford University Press) pp 232–42
[40] Kittel C 1996 *Introduction to Solid State Physics* 7th edn (Toronto: Wiley)
[41] Guzzinati G, Béché A, Lourenço-Martins H, Martin J, Kociak M and Verbeeck J 2017 *Nat. Commun.* **8** 14999
[42] García de Abajo F J 2009 *Phys. Rev. Lett.* **102** 237401
[43] Dlubak B *et al* 2012 *Nat. Phys.* **8** 557
[44] Shi G and Kioupakis E 2015 *Nano Lett.* **15** 6926
[45] Otani Y, Shiraishi M, Oiwa A, Saitoh E and Murakami S 2017 *Nat. Phys.* **13** 829
[46] Joulain K, Mulet J-P, Marquier F, Carminati R and Greffet J-J 2005 *Surf. Sci. Rep.* **57** 59
[47] Greffet J-J and Henkel C 2007 *Contemp. Phys.* **48** 183
[48] Volokitin A I and Persson B N J 2007 *Rev. Mod. Phys.* **79** 1291
[49] Biehs S-A, Tschikin M and Ben-Abdallah P 2012 *Phys. Rev. Lett.* **109** 104301
[50] Biehs S-A, Lang S, Petrov A Y, Eich M and Ben-Abdallah P 2015 *Phys. Rev. Lett.* **115** 174301
[51] Schwinger J 1966 *Phys. Rev.* **152** 1219
[52] Mazzitelli F D, Paz J P and Villanueva A 2003 *Phys. Rev.* A **68** 062106
[53] Hsiang J-T and Lee D-S 2006 *Phys. Rev.* D **73** 065022
[54] Putnam W P and Yanik M F 2009 *Phys. Rev.* A **80** 040902
[55] Kruit P *et al* 2016 *Ultramicroscopy* **164** 31